Dual-Point Refractive Index Measurements Using Coupled Seven-Core Fibers

Natanael Cuando-Espitia, Miguel A. Fuentes-Fuentes, Daniel Alberto May-Arrioja, Iván Hernández-Romano, Rodolfo Martínez-Manuel, and Miguel Torres-Cisneros

***Abstract*—We propose an experimental setup to measure the refractive index (RI) of two independent liquid samples by analyzing a single optical signal. We spliced a section of a seven-core fiber (SCF) into each arm of a 1×2 fiber coupler and spliced additional single mode fiber (SMF) to use as fiber probe tips. As the spatial frequency of the characteristic sinusoidal response of an SCF is a function of the fiber length, we used two different lengths (3 and 10 cm) in our realization. A superluminescent diode (SLD) is used as the light source, and the reflected light by both fiber tips is acquired through an optical circulator. An optical spectrum analyzer (OSA) is used to analyze the spectral response of the combined signals from both fiber tips. We characterized this sensing system by immersing the fiber tips in liquid samples with a RI between 1.3175 and 1.4040. We show that the two independent RI measurements can be retrieved by performing a Fourier transform on the recorded optical spectrum. In particular, we demonstrate that with adequate calibration, the Fresnel coefficients can be calculated independently. The presented approach represents a straightforward and cost-effective fiber implementation for multipoint sensing.**

***Index Terms*—Fresnel reflection, multicore fiber, multipoint measurement, optical fiber sensors, refractive index.**

I. Introduction

During the last decade, the development of fiber optic sensors (FOS) for different applications has attracted a great deal of interest. One of the critical features of FOS is related to the high sensitivity that can be achieved, as compared to other standard techniques. Additionally, taking into account that FOS are made of silica, this allows their operation in environments with strong electromagnetic interference and harsh conditions, as well as high-temperature operation [1], [2]. A variety of sensing applications using FOS have been demonstrated to measure physical variables such as temperature [3], bending [4], stress [5], torsion [6], and refractive index (RI) [7] just to mention a few. Among those applications, the measurement of RI in liquids using FOS is quite important for the development of biosensors [8–10], food industry [11]–[13], and environment monitoring [14]–[16]. In these applications, FOS have additional advantages such as having a small size, and they can also operate using small amounts of liquids, polymers, or both [17]–[19].

The measurement of RI in liquids have been demonstrated using practically every kind of optical fiber and fiber device known to date such as multimode interference (MMI) devices [20], [21], long-period gratings (LPG) [22]–[24], fiber Bragg gratings (FBG) [25], [26], photonic crystal fibers (PCF) [27], [28], tapered or etched multicore fibers (MCF) [29]–[31], capillary fibers [32], Mach-Zehnder interferometers [33], [34], Fabry-Perot interferometers (FPI) [35], [36], Michelson interferometers (MI) [37], [38], and specialty fibers [39], [40]. The sensing mechanism in these configurations relies on the overlap between the propagating optical field and liquid under analysis, which induces a red/blue shift in their spectral response, and the RI is then estimated from this spectral shift. Although good performance and in some cases high sensitivities can be obtained, the main drawback is that the liquid is typically poured and rinsed from the fiber device itself and the risk for damaging the device is quite high. This is particularly important when the fiber has been tapered or etched, as well as when special splicing or complex fabrication procedures are required. A simple solution to this issue is to perform the measurement via the tip of a single mode fiber (SMF) that is connected to the FOS device. In such configuration, the RI is measured via the intensity change that is observed when the fiber tip is submerged into the liquid. The changes in intensity directly modulate the spectral response generated by the FOS device connected to the SMF tip, and thus multiplexing can be easily achieved by using a different spectral response for each SMF tip or channel. The advantage of using the fiber tip as the FOS probe, is that if the tip is damaged, it can be simple cleaved and is ready for use. This is also attractive when measuring polymers that cannot be entirely removed from the tip.

On the other hand, devices exhibiting a spectral bandpass response, such as MMI and LPG, will experience changes in

Manuscript received May 12, 2020; revised July 28, 2020 and August 24, 2020; accepted September 5, 2020. Date of publication September 9, 2020; date of current version January 2, 2021. This work was supported in part by the Mexican National Council of Science and Technology (CONACyT) under Grant CB2016-286368, Grant CB2016-286629, and Grant CB2017-2018-A1-S-31806, in part by Universidad de Guanajuato under Grant CIIC 2020-126 and Grant CIIC 2020-064, in part by the Gobierno del Estado de Guanajuato under SICES Grant AI-20-65, in part by Catedras CONACyT (Project 379), and in part by Postdoctoral Fellowship under Grant 2019-000019-01NACV-00388.
(Corresponding author: Natanael Cuando-Espitia.)

Natanael Cuando-Espitia and Iván Hernández-Romano are with CONACyT-Electronics Department, Sede Palo Blanco, University of Guanajuato, Salamanca, Guanajuato 36885, México (e-mail: natanael.cuando@ugto.mx; hromano@ugto.mx).

Miguel A. Fuentes-Fuentes, Daniel Alberto May-Arrioja, and Rodolfo Martínez-Manuel are with the Centro de Investigaciones en Óptica A. C., Fracc. Reserva Loma Bonita, Aguascalientes 20200, México (e-mail: fuentesma@cio.mx; darrioja@cio.mx; rodolfom@cio.mx).

Miguel Torres-Cisneros is with the Department of Electronics, Universidad de Guanajuato, Guanajuato 36885, México (e-mail: torres.cisneros@ugto.mx).

Color versions of one or more of the figures in this article are available online at https://ieeexplore.ieee.org.

Digital Object Identifier 10.1109/JLT.2020.3022885

their spectral peak intensity as a function of the liquid RI changes [20]–[24]. The main issue for MMI and LPG devices is that if one wants to multiplex them, each fiber tip or channel requires additional spectral bandwidth to separate each channel. In the case of FOS devices that exhibit a sinusoidal spectral response, such as those formed by interferometers, they can be easily adapted to perform RI measurement through an SMF tip [41]. In this way, intensity changes experienced in the SMF tip will directly affect the sinusoidal spectrum. The advantage of this kind of device is that each channel is encoded using a different spatial frequency of the sinusoidal spectra, and their response can be added within the same spectral window. Therefore, by obtaining the Fourier transform of the combined spectral response, the intensity changes in each spectral peak can be observed, and the RI calculated from these intensity changes. The main issue in the case of interferometric devices is related to their complex fabrication procedures that limit the reproducibility of the devices. In this context, devices using MCF have received some attention because their fabrication is simple since they only require splicing a section of MCF between two SMFs to generate the sinusoidal spectral response. Also, their spatial frequency is modified by just changing the length of the MCF section, which requires lengths on the order of centimeters [29]–[31] rather than micrometers as in the case of interferometric devices [42], [43]. In this sense, and in contrast to previously reported refractometers using MCF, we propose here to use the MCF device to encode each sensing channel of a fiber refractometer. We use the fiber tip of a standard SMF, spliced to the MCF for RI measurement, thus allowing us to generate a more robust sensing system. Moreover, the length of the standard SMF does not affect the signal of the proposed sensing head. Therefore, in case of contamination or damage, the tip of the fiber can be easily cleaved, and the new tip of the SMF used for sensing.

In this work, we demonstrate the use of a coupled seven core fiber (SCF) to perform dual-point RI liquid measurements. To better explain such application, we limit our experiment to two channels. Each channel uses a different SCF length, taken care of avoiding exact multiples of the shortest length. The SCF length allows us then to spectrally encode each channel by simply splicing a few centimeters length section of SCF between two SMFs. Therefore, we obtain the RI of the liquid in each channel from the intensity changes of the peaks observed in the Fourier spectrum. Our results demonstrate that the multiplexing of more channels is feasible and without complex fabrication procedures. To the best of our knowledge, this is the first multiplexing application of MCF for RI measurement.

II. Experimental Setup

The Microstructured Fibers and Devices Group at CREOL-UCF provided the SCF used in our experiments. The SCF has seven hexagonal cores, as shown in Fig. 1(a) and Fig. 1(b), with a core and cladding RI of 1.444 and 1.450, respectively. The center-to-center distance between adjacent cores is 12 μm, the separation between the edges is 2 μm, and the edge to edge distance of each core is 9 μm.

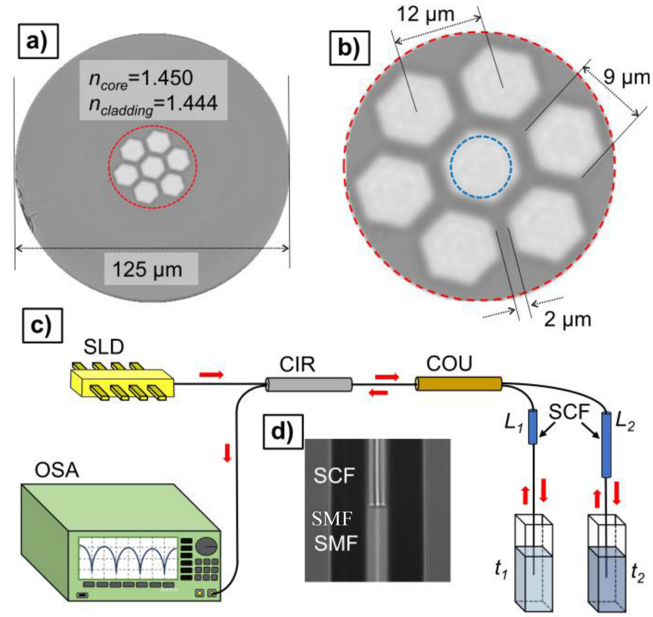

Fig. 1. (a) Transversal section of the SCF used in this work. The fiber diameter is 125 μm and the hexagonal cores are arranged in a honeycomb-like distribution. (b) Detail of the fiber cores showing a separation of 12 μm between center cores. The blue dotted line corresponds to the diameter of the core of the SMF. (c) Schematic representation of the experimental setup consisting on a SLD, an optical circulator (CIR), a 3dB coupler (COU), two sections of SCF (L_1 and L_2). Two fiber tips (t_1, t_2) of SMF are immersed in different liquid samples. The reflected spectrum is recorded by means of an OSA. (d) Image of a SCF-SMF splice taken from the fusion splicer.

The experimental setup for testing our dual-point device is shown in Fig. 1(c). We used a superluminescent diode (SLD) with a spectral bandwidth of 150 nm, ranging from 1460 to 1610 nm, as the optical source. This SLD is used to spectrally interrogate the two arms of a 3 dB coupler. An optical spectrum analyzer (OSA), Anritsu M59740A, was used to capture the combined reflected spectrum coming from the SMF tips. As shown in Fig. 1(c), the SLD optical signal is coupled to port 1 of an optical circulator. The light coming from port 2 is guided to the input of a 1 × 2 coupler operating as a 3 dB coupler. We splice a segment of the SCF to each arm of the coupler by a fusion splicer (Fujikura FSM 60S) using the cladding alignment mode (see Fig. 1(d)). Then, a segment of standard SMF is spliced to the SCFs generating two SMF-SCF-SMF structures. It is important to remember that the SCF length in each SMF-SCF-SMF structure is different. The reflected signals from these sensing probes are directed through port 3 of the circulator and measured with the OSA. Finally, the combined spectrum is processed and analyzed to obtain the RI of both liquids.

Notice that an important advantage of SMF-MCF-SMF structures is their straightforward construction based on the direct splicing by commercial splicers. Moreover, similar fiber structures obtained by direct splicing have been used in simultaneous force-temperature measurements [44] as well as in curvature [45], strain [46], [47], high sensitivity RI [7], [31] and high temperature sensing [48].

III. Principle of Operation

The mode-coupled theory is typically used to study MCFs in which their cores are closely packed, and thus strong coupling is present [49]–[51]. The basic idea under this approach is that the resulted modal structure (supermodes) of such waveguides consists on the supported individual eigenmodes of each core which also obeys $dA/dz = i\boldsymbol{M}A$ where z is the propagation direction, *A* is the vector of complex amplitudes and ***M*** is the coupling matrix [52], [53]. Previous reports have shown experimentally and theoretically that in an SMF-MCF-SMF structure, and due to their circular symmetry, the interaction occurs mainly between the central core of the MCF and the core of the SMF; or correspondingly, between the supermodes associated to the central core of the MCF and the fundamental mode of the SMF [45], [54]–[56]. According to mode-coupled theory, the coupling coefficient between identical cores of radius ρ and separated a distance *d* in a centro-symmetric MCF is [49]–[51]:

$$\kappa = \frac{\sqrt{\delta}}{\rho}\frac{U^2}{V^3}\frac{K_0\left[Wd/\rho\right]}{{K_1}^2\left[W\right]} \tag{1}$$

Here, K_0 and K_1 are the modified Hankel functions of order 0 and 1, respectively. The contrast between the RI of the core (n_{core}) and the RI of the cladding ($n_{cladding}$) is considered in Eq. (1) by the factor $\delta = 1 - (n_{cladding}/n_{core})^2$. The normalized transverse propagation constants in the core and cladding are represented in Eq. (1) as *U* and *W* respectively, and are related to the parameter *V* by $V^2 = U^2 + W^2$. In addition, the parameter *V* is defined as:

$$V^2 = \left(\frac{2\pi\rho n_{core}}{\lambda}\right)^2\delta \tag{2}$$

where λ is the wavelength of light in vacuum. Moreover, the complex amplitude of the central mode for a configuration with six outer cores, and when we launch light into the central core is [57], [58]:

$$A = e^{i\kappa L}\left[\cos\left(\sqrt{7}\kappa L\right) - \frac{i}{\sqrt{7}}\sin\left(\sqrt{7}\kappa L\right)\right] \tag{3}$$

where *L* is the length of the SCF. Previous work on hexagonal cores-MCF has shown a good agreement between the experimental results and coupled-mode theory assuming circular cores [31], [44], [48], [59]. Based on these reports, we have considered circular cores on Eqs. (1)–(3) as an appropriate approximation for the experimental hexagonal cores-MCF.

We can simplify the coupling coefficient κ in Eq. (3) by noticing its linear dependence within the region of interest of this study (1490 nm-1590 nm) and for the values of the experimental constants detailed in the previous section. Fig. 2 shows the calculated coupling coefficient using Eq. (1) as a solid blue line.

The solid blue line shown in Fig. 2 was calculated using $n_{core} = 1.450$, $n_{cladding} = 1.444$, $\rho = 4.5$ μm, and $d = 12$ μm. Fig. 2 also shows a linear approximation of κ based on a power series expansion around $\lambda_0 = 1540$ nm as a black dotted line. The approximation of the coupling coefficient (κ') effectively overlaps the calculated κ values using Eq. (1) in the region of interest. The linear approximation in the expansion form is:

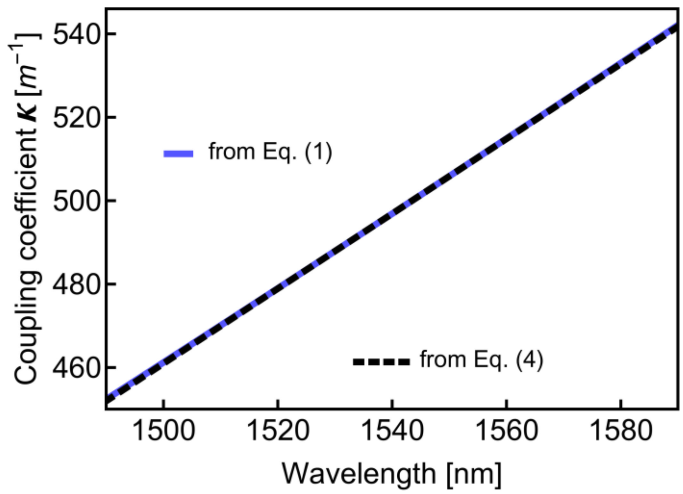

Fig. 2. Coupling coefficient between cores (κ) as function of wavelength. The solid blue line represents the coupling coefficient obtained by means of Eq. (1) whereas the black dotted line represents a linear approximation based on a power series expansion as shown in Eq. (4).

$$\kappa' = a + b\left(\lambda - \lambda_0\right) \tag{4}$$

with $a = 496.85$ m^{-1}, $b = 8.97 \times 10^8$ m^{-2} and $\lambda_0 = 1540$ nm. Substituting Eq. (4) in Eq. (3) and assuming *a*, *b*, λ, λ_0 and z as real values, the normalized power of the central mode $|A|^2$ is:

$$|A|^2 = \cos^2\left[\sqrt{7}L\left(a + b(\lambda - \lambda_0)\right)\right] + \frac{1}{7}\sin^2\left[\sqrt{7}L\left(a + b(\lambda - \lambda_0)\right)\right]. \tag{5}$$

Then, using $\cos^2\theta + \sin^2\theta = 1$ and $2\cos^2\theta - 1 = \cos 2\theta$ and rearranging terms, $|A|^2$ can be expressed as:

$$|A|^2 = \frac{1}{7}\left[4 + 3\cos\left(\alpha + \beta\lambda\right)\right] \tag{6}$$

where $\alpha = \sqrt{7}L(a - b\lambda_0)/\pi$ and $\beta = \sqrt{7}Lb/\pi$. Notice that α corresponds to a phase shift in the periodic response of the SCF while β corresponds to the spatial frequency of the SCF. In Eq. (6) the argument of the cosine function was multiplied by $1/2\pi$ in order to express the spatial frequency β in cycles/μm instead of rad/μm. Fig. 3(a) depicts the normalized power for two different fiber lengths (3 and 10 cm). The normalized power depicted in Fig. 3(a) can be interpreted as the optical power transmitted in an SMF-SCF-SMF device with an SCF of length *L*.

Fig. 3(a) shows a sinusoidal response of around two cycles within the 100 nm plotted for the SFC of 3 cm (blue curve). This can be explained as $\beta_{3cm} = \sqrt{7}$ (0.03)(8.97 $\times$ 10^8)/$\pi \approx$ 22.7 cycle/μm which also equals 2.27 cycle/100 nm. In contrast, the corresponding response of the SCF of 10 cm (red curve) shows a higher frequency response of about seven cycles within the plotted range of Fig. 3(a) as $\beta_{10cm} = \sqrt{7}$ (0.1)(8.97 $\times$ 10^8)/π $\approx$ 75.6 cycle/μm or 7.56 cycle/100 nm.

However, the experimental setup shown in Fig. 1 relies on the detection of the light reflected from the tip of the fibers. In other words, the light injected in each arm of the coupler

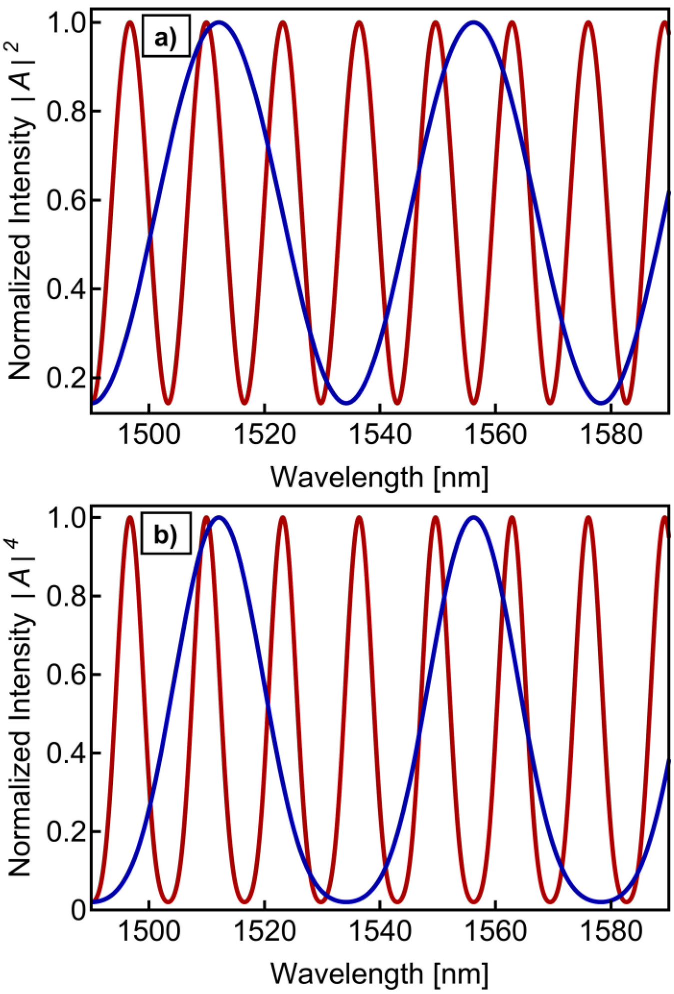

Fig. 3. Normalized intensity of an SCF ($n_{core} = 1.450$, $n_{cladding} = 1.444$, $\rho = 4.5$ μm and $d = 12$ μm $R_t = 1$) with two different lengths (L) in transmission *(a)* and in reflection *(b)*. Transmission curves were generated using Eq. (6) while reflected curves were generated using Eq. (7). The dark blue curves corresponds to a SCF with $L_1 = 3$ cm. On the other hand, the dark red curves corresponds a SCF with $L_2 = 10$ cm.

in Fig. 1 passes through the corresponding SCF segment twice before reaching the OSA. The reflected intensity in each arm of the coupler is then proportional to $|A|^4$. Using Eq. (6) and $2\cos^2\theta - 1 = \cos 2\theta$, the reflected intensity in an SCF is given by:

$$|A|^4 = \frac{R_t}{98}\left[41 + 48\cos\left(\alpha + \beta\lambda\right) + 9\cos\left(2\alpha + 2\beta\lambda\right)\right] \quad (7)$$

In Eq. (7) the constant R_t is determined by the Fresnel reflection experienced at the tip of the fiber. Notice that in Eq. (7) a harmonic component at 2β arises as the light passes twice through the SCF. Fig. 3(b) shows the reflected spectra of two SMF-SCF-SMF structures with $L_1 = 3$ cm and $L_2 = 10$ cm. The number of oscillations in the curves depicted in Fig. 3(b) coincides with their transmission counterparts (Fig 3(a)) as the dominant oscillatory component in the expressions of Eq. (6) and Eq. (7) is a cosine function at $\alpha + \beta\lambda$. However, the curves in Fig. 3(b) exhibit slightly sharper crests and wider troughs as the expression of Eq. (7) contains a small harmonic component at $2\alpha + 2\beta\lambda$.

After traveling back from the tips of the fibers, the light beams from both arms are combined in the coupler [60], reach the circulator, and are then analyzed by the OSA. In general, the intensity I of two superimposed optical signals I_1, I_2 of quasi-monochromatic light can be obtained as follows [61]:

$$I = I_1 + I_2 + 2\sqrt{I_1 I_2}\,|\gamma_{12}(OPD)|\cos\left(2\pi\frac{OPD}{\lambda_0}\right) \quad (8)$$

In Eq. (8), γ_{12} represents the complex degree of coherence, OPD is the optical path difference and λ_0 is the central wavelength of the source. When the OPD is larger than the coherence length of the optical source ($l_c = 2\ln 2\, \lambda_0^2/\Delta\lambda$) the third term of Eq. (8) vanishes [62]. In the experiment (see Fig 1), the sensing arms of the coupler have the same length of SMF in each arm; then, an optical path difference (OPD) of several centimeters ($\sim$7 cm) is generated by the segments of the SCF. Moreover, the SLD used in these experiments is centered at $\lambda_0 = 1535$ nm and has a full width at half maximum of $\Delta\lambda = 150$ nm; resulting in a l_c of 7 μm. Having an OPD of centimeters and using an SLD as an optical source, we make sure not to have a Michelson-interferometer effect coming from the sensing arms of the fiber coupler, and the output intensity reaching the OSA can be written as:

$$I_{out} = |A_{t1}|^4 + |A_{t2}|^4 \quad (9)$$

In Eq. (9) $|A_{t1}|^4$ represents the intensity reflected back from t_1 which in turn correspond to the arm with a SCF segment of 3cm ($L_1 = 3$ cm). Similarly, $|A_{t2}|^4$ represents the intensity reflected back from t_2 which corresponds to the arm with a segment of 10 cm of SCF ($L_2 = 10$ cm). Notice that for the proposed experimental setup, Eqs. (7) and (9) implies that 4 frequency components are expected in I_{out} provided that $L_2 > 2L_1$. Moreover, and according to Eq. (7), the amplitude of each pair of components will be governed by the Fresnel reflection experienced in each fiber tip. This means that information about the RI of the media surrounding both fiber tips is encoded within the amplitude of the corresponding frequency components. Therefore, two independent refractive indices can be extracted from a single signal by conventional frequency domain analysis.

IV. Results

As detailed in the experimental setup section, the experiments are based on the spectral analysis of an optical beam coming from two independent fiber tips immersed in different liquid samples. The liquid samples were prepared by mixing deionized water (DW) and glycerol in different weight fractions. Table I shows the glycerol content of the samples prepared in this study and the calculated RI at 1550 nm as in [63].

As shown in Table I, the RI of the liquid samples range from 1.3175 to 1.404. The glycerol content of the prepared samples was chosen to obtain RI steps of 0.0173. Both fiber tips were vertically mounted in linear stages and were cleaned with acetone before immersing in the subsequent liquid sample. As schematically shown in Fig. 1, the samples were allocated in

TABLE I
REFRACTIVE INDEX OF DEIONIZED WATER AND GLYCEROL SOLUTIONS

Sample	Glycerol content (wt. %)	Refractive index at 1550 nm
S_1	0	1.3175
S_2	11.54	1.3348
S_3	23.08	1.3521
S_4	34.62	1.3694
S_5	46.15	1.3867
S_6	57.69	1.4040

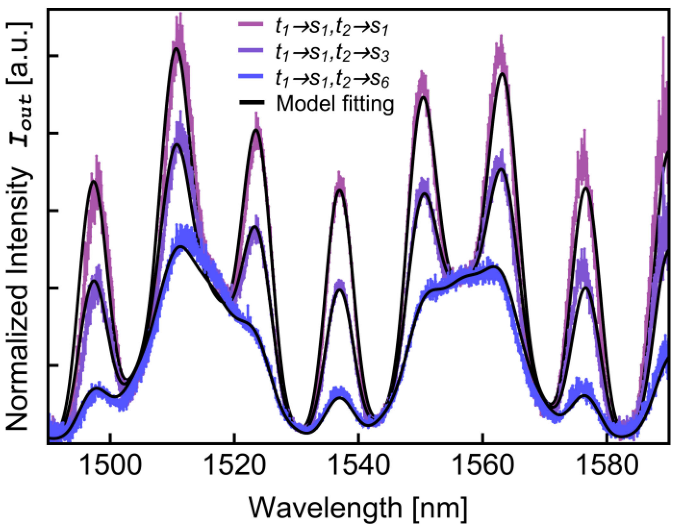

Fig. 4. Recorded spectra from the experimental setup. The three different spectra data correspond to different liquid samples in t_2 tip and in t_1 tip. The solid black lines correspond to model-fitting curves based on Eq. (7) and Eq. (9). A good agreement between the data and model is evident.

commercial cuvettes using 3.5 ml of the corresponding sample. Notice also that S_1 corresponds to the sample with the lowest RI whereas S_6 corresponds to the sample with the highest RI. All the recorded spectra were normalized by the spectral response of the light source in order to obtain the normalized intensity I_{out}.

During all the experiments, the laboratory temperature was set at 25°C and a cuvette holder was used to avoid temperature instabilities. Fig. 4 shows three representative recorded spectra in which tip t_1 was kept immersed in S_1 whereas tip t_2 was immersed in S_1, S_3 and S_6.

In addition to experimental data, Fig. 4 shows model fitting curves based on Eqs. (7) and Eq. (9) depicted as black solid line for each experimental curve. The model fitting was performed by applying the Newton method and considering the experimental constants values as detailed in previous sections.

Then, the corresponding constants R_t from Eq. (7) and a phase shift between signals from both fiber tips were considered as free parameters. As seen in Fig. 4, the model fitting correlate well with the experimental curves supporting the analysis performed in Section II.

In general, the curves of Fig. 4 indicate that as the RI at t_2 increases, the experimental response tend to a periodic curve

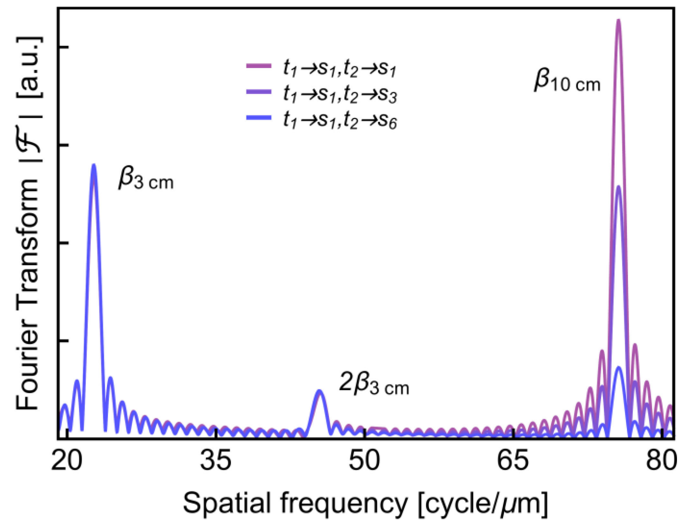

Fig. 5. Absolute value of the Fourier transforms of the model-fitted curves shown in Fig. 4. Three peaks can be clearly distinguished. These peaks correspond to the frequency terms of Eq. (6); $\beta_{3cm} = 22.7$ cycle/μm, $2\beta_{3cm} = 45.4$ cycle/μm and $\beta_{10cm} = 75.6$ cycle/μm.

of lower frequency comparing to the curve when both tips are immersed in sample S_1. As the RI at t_2 increases, the RI contrast between the fiber and the liquid sample decreases. This in turn decreases the amount of light reflected at the fiber-liquid interface of t_2 and letting the low frequency signal reflected from t_1 to dominate over the resulted curve. This behavior can be observed in Fig. 5.

Fig. 5 shows the Fourier transform of the model-fitted curves shown in Fig. 4. The model-fitted curves of Fig. 4 were Fourier transformed and convoluted with the response of the OSA. Then, the absolute value of the resulted Fourier transform is plotted in Fig. 5 using the same color labeling used in Fig. 4. The Fourier transformed curves shown in Fig. 5 displays three main frequency peaks at 22.7, 45.4 and 75.6 cycle/μm. However, only the 75.6 cycle/μm component exhibits important variation while the 22.7 and 45.4 cycle/μm peaks shows the same amplitude over the plotted curves. The 22.7 and 45.4 cycle/μm peaks correspond to the fundamental and harmonic spatial frequencies for $L = 3$ cm (β_{3cm}, $2\beta_{3cm}$), respectively. On the other hand, the peak at 75.6 cycle/μm corresponds to the fundamental spatial frequency for $L = 10$ cm (β_{10cm}). The harmonic component for $L = 10$ cm ($2\beta_{10cm}$) at 151.2 cycle/μm is out the plotted frequency range in Fig. 5 as we have centered our attention on the fundamental frequencies which present a larger change in component amplitude.

Fig. 5 shows that the β_{10cm} component decreases as the RI at t_2 increases and moves closer to the RI of the fiber core. Conversely, the β_{3cm} and $2\beta_{3cm}$ components show almost no variation when the RI at t_2 changes. This result indicates that the information from two independent refractive indices measurements can be effectively recovered from a single signal.

In order to further explore the proposed sensing approach, we fixed the RI at t_2 and vary the RI of the sample at t_1. Fig. 6 shows the recorded spectra and absolute values of the Fourier

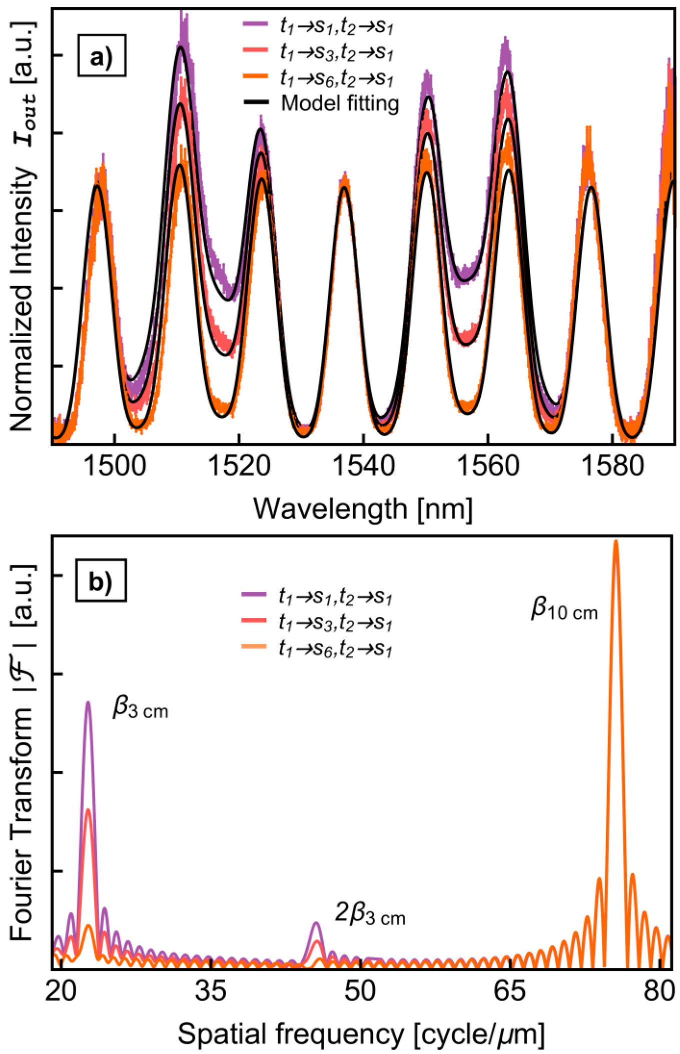

Fig. 6. Recorded spectra (a) and Fourier transforms (b) from experiments with t_1 immersed in samples S_1, S_3 and S_6 and constant RI in t_2 (S_1). In contrast with Fig. 4 and Fig. 5, Fig. 6 shows a variation on the β_{3cm} and $2\beta_{3cm}$ components and a steady β_{10cm} spatial frequency component.

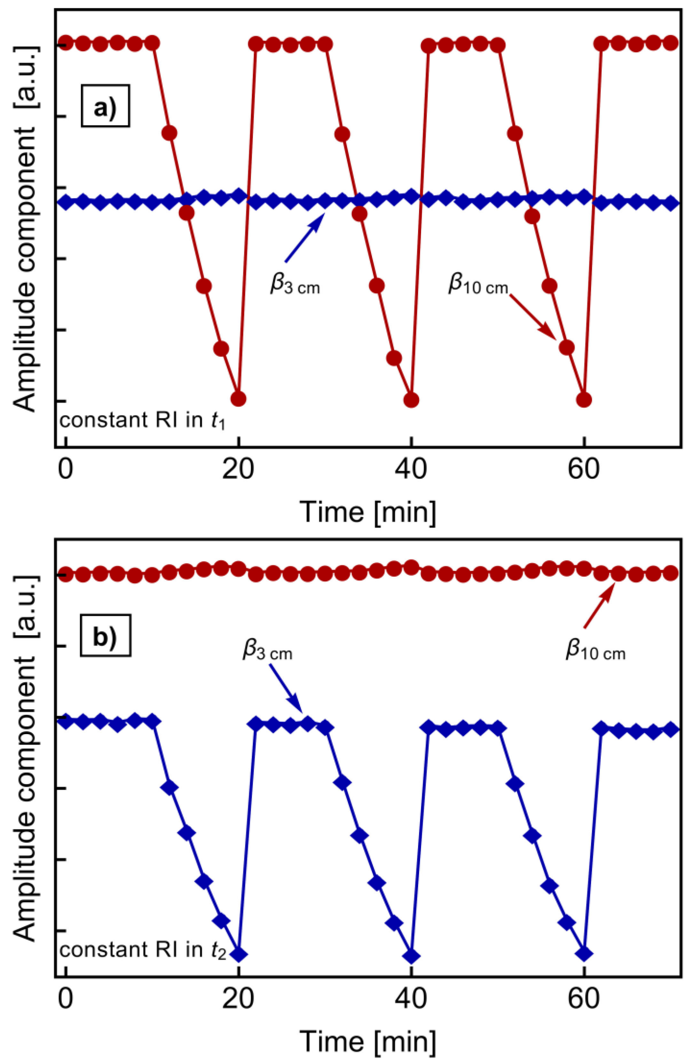

Fig. 7. Amplitude of the β_{3cm} and β_{10cm} spatial frequency components during the repeatability tests. a) Repeatability test with constant RI at t_1 and variation on the RI at t_2. b) Repeatability test with constant RI at t_2 tip and variation on the refractive index at t_1. In both tests the RI variation in the corresponding fiber tip occurs during three time intervals: 10–20 min, 30-40 min and 50-60 min. During each time interval the six liquid samples were probed.

transform from these set of experiments. As expected, Fig. 6 depicts the opposite behavior of Fig. 5 by decreasing the β_{3cm} and $2\beta_{3cm}$ components as the RI at t_1 increases while showing a steady β_{10cm} component.

We also explored the repeatability (see Fig. 7) of the proposed approach by performing consecutive RI measurements with one of the fiber tips immersed in S_1 and varying the RI at the tip of the remaining fiber tip.

The test started with both fibers immersed in S_1 during 10 minutes. During these initial 10 minutes, a spectrum was recorded each 2 minutes. Then, one of the fibers was immersed in S_2, S_3, S_4, S_5 and S_6 in that order. The corresponding spectrum of each liquid sample was acquired after immersion in steps of two minutes. A total of six measurements corresponding to different refractive indices were obtained between minute 10 and minute 20. Then, both fiber tips were immersed again in S_1 and the cycle started again. The test was stopped after completion of three cycles. During the entire test, the remaining fiber tip was kept immersed in S_1. Then, the fiber tips were interchanged and the test was repeated. The results of these tests are summarized in Fig. 7.

The acquired spectra were model-fitted and Fourier transformed as previously detailed. Then, the amplitude of the β_{3cm} and β_{10cm} components were extracted from the absolute value of the Fourier transform. The amplitude of the β_{3cm} component (dark blue diamonds) as well as the amplitude of the β_{10cm} component (dark red circles) are plotted as function of time in Fig. 7. In particular, Fig. 7(a) shows the amplitude of the extracted components for the case in which the RI at t_1 was kept constant and the RI at t_2 was varied; there, the β_{10cm} component decreases during three time intervals, namely: 10–20, 30–40 and 50–60 minutes. These time intervals coincide with the time intervals in which the RI at t_2 was varied. Figure 7(a) also shows that the β_{3cm} component presents very small changes

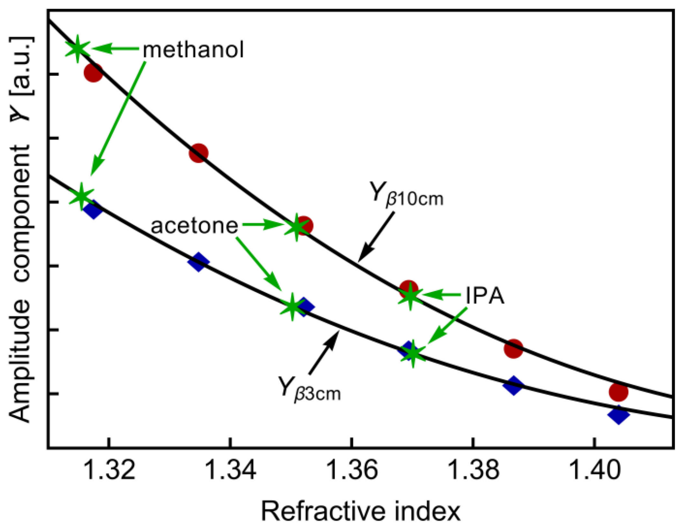

Fig. 8. Amplitude of the β_{3cm} and β_{10cm} spatial frequency components as function of RI. The circle and diamond symbols represent the mean value shown in Fig. 7. Solid black lines correspond to model-fitting curves based on a modified Fresnel coefficient. Green star symbols correspond to the mean value of RI measurements of methanol, acetone and IPA (see Table II).

over the entire test. On the other hand, Fig. 7(b) shows important variations on the β_{3cm} component and very small variations on the β_{10cm} component. Moreover, the variation of the β_{3cm} component in Fig. 7(b) displays a similar behavior of the β_{10cm} component of Fig 7(a). In both cases, a periodic behavior is seen which coincides with the variation of the RI on the corresponding fiber tip. Furthermore, Fig. 7 shows good repeatability in the measurements performed with both fiber tips studied here.

In order to observe the dependence of the β_{3cm} and β_{10cm} components on the RI of the liquid samples, we have plotted the amplitude component Y as a function of the RI of the probed reference samples. Each point in Fig. 8 corresponds to the mean value of at least three experimental measurements and the standard deviation for all points shown is smaller than the corresponding symbols. Furthermore, Fig. 8 shows two black solid lines corresponding to the following equation:

$$Y_{\beta 3cm,\beta 10cm} = C_{1,2}\left|\frac{1.45 - n_{1,2}}{1.45 + n_{1,2}}\right|^2 + g_{1,2} \tag{10}$$

In Eq. (10), $Y_{\beta 3cm}$ and $Y_{\beta 10cm}$ refer to the amplitude of β_{3cm} and β_{10cm} components, respectively. The RIs at t_1 and t_2 are labeled in Eq. (10) as n_1 and n_2, respectively. The constants C and g in Eq. (10) were used as free parameters to obtain the best-fitting curve to experimental data. Fig. 8 shows that the model correlates well with the obtained data. Interestingly, the right hand side of Eq. (10) can be seen as a modified Fresnel coefficient as the expression contains a correction factor C, the reflection Fresnel coefficient for normal incidence and a constant g as an extra term. These constants are related to the losses generated at the splices of the experimental setup and thus are not considered within the conventional Fresnel coefficient derivation. The constant g accounts for the amount of light that is reflected by the splices. Once the fiber setup is spliced and provided constant power in the light source, the amount of light reflected for RI matching conditions is also constant.

TABLE II
MEASURED RI OF METHANOL ACETONE AND ISOPROPANOL

Sample	Ref. [49]	$\bar{n}_1$±SD	$\bar{n}_1$ % error	$\bar{n}_2$±SD	$\bar{n}_2$ % error
Methanol	1.3174	$1.3155\pm4\cdot10^{-4}$	0.14	$1.3149\pm3\cdot10^{-4}$	0.19
Acetone	1.3483	$1.3502\pm6\cdot10^{-4}$	0.14	$1.3509\pm9\cdot10^{-4}$	0.20
IPA	1.3661	$1.3701\pm3\cdot10^{-4}$	0.29	$1.3697\pm3\cdot10^{-4}$	0.26

On the other hand, once the light interacts with the liquid sample, an amount of light is reflected back according to the Fresnel coefficient. However, before reaching the OSA the light passes again through the splicing sites losing an amount of light due to splice imperfections and geometric differences between the cores of the SMF and SCF. In this sense, once the fiber device is spliced, the amount of light lost by the splicing sites is proportional to the light reflected at the liquid-fiber interface. Then, the correction factor C multiplying the Fresnel coefficient in Eq. (10) accounts for losses experienced by the light from the fiber tip to the OSA. In general, the effect of the splices is device dependent. Thus, as the parameters C and g are related to the intrinsic device characteristics, these parameters can be used as calibration parameters for each sensing fiber tip.

Finally, we have tested the proposed dual-point RI sensor by measuring the RI of three well-known solvents: methanol, acetone and isopropanol (IPA). The solvents were purchased from Thermo Fisher Scientific (MA, USA) with >99.5% purity. Refractive indexes of tested solvents at 1550 nm and 298 K can be found in [64]. The solvents were allocated in the quartz cuvettes and the fiber tips were immersed in the cuvettes. The 9 possible configurations of solvents in each fiber tip were tested (methanol-methanol, methanol-acetone, methanol-IPA, acetone-methanol, acetone-acetone, acetone-IPA, IPA-methanol, IPA-acetone and IPA-IPA). For each configuration of solvents, 3 measurements were recorded resulting in a total set of 27 recorded measurements. Then, the amplitude components $Y_{\beta 3cm}$ and $Y_{\beta 10cm}$ were calculated for each recorded signal. Once the calibration parameters C and g are determined and considering the fact that n_{core} is higher than the RIs at t_1 and t_2, one can solve Eq. (10) for $n_{1,2}$ as function of the amplitude components $Y_{\beta 3cm}$ and $Y_{\beta 10cm}$ as follows:

$$n_{1,2} = \frac{1.45\left(C_{1,2} + Y_{\beta 3cm,\beta 10cm} - g_{1,2}\right)}{C_{1,2} + g_{1,2} - Y_{\beta 3cm,\beta 10cm}} - \frac{2.9\sqrt{C_{1,2}\left(Y_{\beta 3cm,\beta 10cm} - g_{1,2}\right)}}{C_{1,2} + g_{1,2} - Y_{\beta 3cm,\beta 10cm}}. \tag{11}$$

The RIs were thus retrieved based on Eq. (11) for all the measured optical signals. Then, the results were grouped and the mean values and standard deviation (SD) of the measurements were calculated. Table II summarizes the results from these set of experiments.

In Table II the mean value of the RI measured at t_1 is indicated as n_1 whereas the mean value of RI measured at

t_2 is indicated as n_2. The error for $n_{1,2}$ was computed as $100 \times |(\bar{n}_{1,2} - n_{ref})/n_{ref}|$, where n_{ref} is the corresponding RI of the tested solvent according to [49]. The mean values of the measured RIs are also showed in Fig. 8 as green stars symbols. The highest error registered was 0.29% and the larger SD was 0.0009 RIU. In general, Table II demonstrates a good correspondence of the proposed sensor with previously reported RIs of the tested solvents at 1550 nm. Moreover, data of Table II shows a remarkable repeatability of the proposed sensor.

V. Discussion

In this paper, we demonstrate that using the proposed configuration two independent RI measurements can be obtained by means of a single optical signal. Moreover, with the correct calibration the reflection Fresnel coefficients can be retrieved from each fiber tip. Although the number of sensing fiber tips used in this study was limited to two in order to demonstrate the feasibility of the proposed approach, is evident that the principle of operation allows for n number of sensors which only need to be separated in their spatial frequencies. A more extensive multipoint sensor based on the approach presented here should consider a precise spatial frequency design in order to maximize the available frequency spectrum.

On the other hand, notice that in contrast with conventional multipoint fiber sensing schemes, the proposed configuration prevents the use of fiber Bragg gratings (FBG) or fiber interferometric constructions such as Fabry-Perot, Michelson or Mach-Zehnder interferometers. In other words, the proposed approach replaces the use of expensive FBG or complicated interferometric setups with a section of a SCF which is spliced into commercial SMF. Also, different to fiber refractometers using specialty fiber such as PCF, MCF, and no-core fiber as part of a sensing head, in the proposed configuration the SCF is used only to encode the signal from each sensing tip. Therefore, the SCF does not need to be in close proximity to the fiber tip, allowing for easy implementation of the fiber tip as a dip-probe sensing head. We can also consider the advantage of having a system with a disposable sensing head since the fiber in contact with the sensing liquid consist on commercial SMF. In this respect, if the fiber tip gets damage or contaminated, it can be cut, dispose, and the new tip easily calibrated to be implemented without affecting the performance of the multipoint sensor. Furthermore, the characteristic sinusoidal response of the SCF can be easily tuned just by adjusting the length of the spliced SCF in the range of centimeters.

As shown in Fig. 4 and Fig. 6(a), the recorded spectra contain a reasonable amount of noise as only a small proportion of the inyected light is reflected back and reaches the OSA. Although noise-reduction methods could be applied, we have observed that these methods result in similar results compared to the model-fitting using the normalized raw spectra. Fig. 9 shows a noise-reducted spectrum and the corresponding fitting based on Eq. (6).

Fig. 9 shows a normalized spectrum in which a moving average of 20 points was applied to smooth the experimental curve. However, the fitted curve in Fig. 9 is almost identical to the curve obtained using the un-processed normalized spectrum. Furthermore, the calibration curves based on the smoothed spectra are shown in the inset of Fig. 9, which are also very similar to their counterparts based on normalized raw spectra (see Fig. 8). Therefore, the proposed method used to obtain the fitting curve is actually accurate and permits multipoint RI measurements with the proposed configuration.

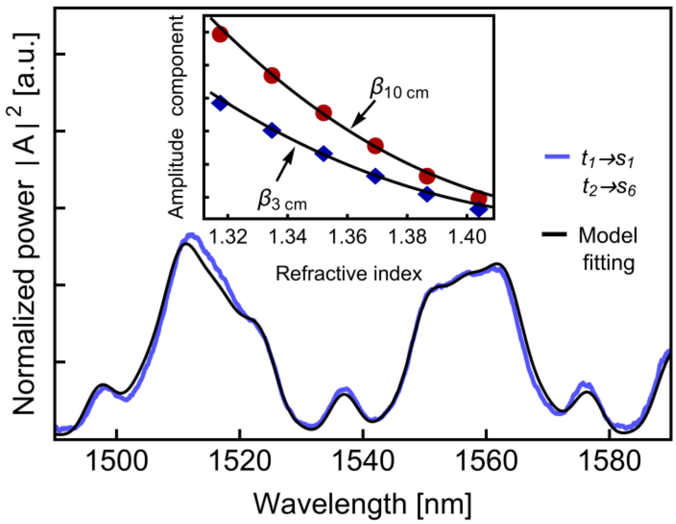

Fig. 9. Smoothed experimental spectrum and its corresponding fitting curve based on Eq. (6). A moving average of 20 points was performed on a raw normalized spectrum when t_1 is immersed in S_1 and t_2 immersed in S_6. The inset shows the amplitude of the β_{3cm} and β_{10cm} spatial frequency components as function of RI using smoothed spectra.

It is worth to mention that the analysis of the experimental results presented here assumes that the RI of the liquid samples is lower than the RI of the fiber core; and the current experimental setup is unable to distinguish between RIs above or below the RI of the fiber core. However, the uncomplicated realization of the experimental setup allows us to further investigate how to overcome this limitation.

VI. Conclusion

A simple configuration of a multipoint RI sensor was proposed and demonstrated. The sensor was based on sections of SCF spliced between commercial SMF. By employing different lengths of the SCF, the information about the RI at the corresponding fiber tip was spatially frequency encoded. A conventional Fourier analysis was performed to retrieve the corresponding Fresnel coefficient. The SMF is used as the sensing head, and allows for a disposable sensing head system, as in case of damage or contamination the fiber tip can be cleaved and easily calibrated to use it as the new sensing head. The proposed approach present advantages as straightforward design and inexpensive fiber devices. Nevertheless, the limitation of the current experimental setup is the ambiguity for liquid RI below and above the RI of the fiber core and forthcoming investigations in our group will address this limitation. The study presented here can be seen as starting point for the development of more robust multipoint fiber sensors based on highly coupled SCF.

ACKNOWLEDGMENT

The authors acknowledge the Microstructured Fibers and Devices Group at CREOL-UCF for kindly providing the SCF used in this work.

REFERENCES

[1] G. Rajan and K. K. Iniewski, " Optical fiber sensors: Advanced techniques and applications," in *Optical Fiber Sensors: Advanced Techniques and Applications*. Boca Raton, FL, USA: Taylor & Francis, 2017.

[2] N. Sabri, S. A. Aljunid, M. S. Salim, and S. Fouad, *Recent Trends in Physics of Material Science and Technology*. Springer Singapore, Singapore, 2015, vol. 204.

[3] A. Van Newkirk, E. Antonio-Lopez, G. Salceda-Delgado, R. Amezcua-Correa, and A. Schülzgen, "Optimization of multicore fiber for high-temperature sensing," *Opt. Lett.*, vol. 39, no. 16, 2014, Art. no. 4812.

[4] K. Yang *et al.*, "Femtosecond laser inscription of fiber Bragg grating in twin-core few-mode fiber for directional bend sensing," *J. Lightw. Technol.*, vol. 35, no. 21, pp. 4670–4676, Nov. 2017.

[5] M. A. S. Zaghloul *et al.*, "Discrimination of temperature and strain in brillouin optical time domain analysis using a multicore optical fiber," *Sensors*, vol. 18, no. 4, pp. 1176-1–1176-9, 2018.

[6] F. Tan, Z. Liu, J. Tu, C. Yu, C. Lu, and H.-Y. Tam, "Torsion sensor based on inter-core mode coupling in seven-core fiber," *Opt. Express*, vol. 26, no. 16, 2018, Art. no. 19835.

[7] J. R. Guzmán-Sepúlveda, R. Guzmán-Cabrera, M. Torres-Cisneros, J. J. Sánchez-Mondragón, and D. A. May-Arrioja, "A highly sensitive fiber optic sensor based on two-core fiber for refractive index measurement," *Sensors*, vol. 13, no. 10, pp. 14200–14213, 2013.

[8] H. Tazawaa, T. Kanie, and M. Katayama, "Fiber-optic coupler based refractive index sensor and its application to biosensing," *Appl. Phys. Lett.*, vol. 91, no. 11, 2007, Art. no. 113901.

[9] M. I. Zibaii, A. Kazemi, H. Latifi, M. K. Azar, S. M. Hosseini, and M. H. Ghezelaiagh, "Measuring bacterial growth by refractive index tapered fiber optic biosensor," *J. Photochemistry Photobiol. B: Biol.*, vol. 101, no. 3, pp. 313–320, 2010.

[10] L. Rindorf and O. Bang, "Sensitivity of photonic crystal fiber grating sensors: Biosensing, refractive index, strain, and temperature sensing," *JOSA B*, vol. 25, no. 3, pp. 310–324, 2008.

[11] H. A. Razak, N. H. Sulaiman, H. Haroon, and A. S. Mohd Zain, "A fiber optic sensor based on Mach–Zehnder interferometer structure for food composition detection," *Microw. Opt. Technol. Lett.*, vol. 60, no. 4, pp. 920–925, 2018.

[12] N. Bidin, N. H. Zainuddin, S. Islam, M. Abdullah, F. M. Marsin, and M. Yasin, "Sugar detection in adulterated honey via fiber optic displacement sensor for food industrial applications," *IEEE Sens. J.*, vol. 16, no. 2, pp. 299–305, Jan. 2016.

[13] A. Gowri, A. S. Rajamani, B. Ramakrishna, and V. V. R. Sai, "U-bent plastic optical fiber probes as refractive index based fat sensor for milk quality monitoring," *Opt. Fiber Technol.*, vol. 47, no. 1, pp. 15–20, 2019.

[14] K. R. Rogers and E. J. Poziomek, "Fiber optic sensors for environmental monitoring," *Chemosphere*, vol. 33, no. 6, pp. 1151–1174, 1996.

[15] H. Joe, H. Yun, S. Jo, M. B. Jun, and B. K. Min, "A review on optical fiber sensors for environmental monitoring," *Int. J. Precis. Eng. Manuf.-Green Tech.*, vol. 5, no. 1, pp. 173–191, 2018.

[16] S. Muto, O. Suzuki, T. Amano, and M. Morisawa, "A plastic optical fibre sensor for real-time humidity monitoring," *Meas. Sci. Technol.*, vol. 14, no. 6, pp. 746–750, 2003.

[17] P. Nath, H. K. Singh, P. Datta, and K. C. Sarma, "All-fiber optic sensor for measurement of liquid refractive index," *Sens. Actuators A: Phys.*, vol. 148, no. 1, pp. 16–18, 2008.

[18] B. H. Lee *et al.*, "Interferometric fiber optic sensors," *Sensors*, vol. 12, no. 3, pp. 2467–2486, 2012.

[19] A. Leung, P. M. Shankar, and R. Mutharasana, "A review of fiber-optic biosensors," *Sens. Actuators B: Chemical*, vol. 125, no. 2, pp. 688–703, 2007.

[20] C. Guo, P. Niu, J. Wang, J. Zhao, and Ch. Zhang, "Dual-point reflective refractometer based on parallel no-core fiber/FBG structure," *Opt. Fiber Technol.*, vol. 40, pp. 46–51, 2018.

[21] J. E. Antonio-Lopez, D. A. May-Arrioja, and P. LiKamWa, "Fiber-optic liquid level sensor," *IEEE Photon. Technol. Lett.*, vol. 23, no. 23, pp. 1826–1828, Dec. 2011.

[22] G. Quero *et al.*, "Evanescent wave long-period fiber grating within D-shaped optical fibers for high sensitivity refractive index detection," *Sens. Actuators B*, vol. 152, no. 2, pp. 196–205, 2011.

[23] L. Coelho, D. Viegas, J. L. Santos, and J. M. M. M. de Almeida, "Enhanced refractive index sensing characteristics of optical fibre long period grating coated with titanium dioxide thin films," *Sens. Actuators B*, vol. 202, pp. 929–934, 2014.

[24] X. Chen, J. Xu, X. Zhang, T. Guo, and B. Guan, "Wide range refractive index measurement using a multi-angle tilted fiber Bragg grating," *IEEE Photon. Technol. Lett.*, vol. 29, no. 9, pp. 719–722, May 2017.

[25] D. Luo, J. Ma, Z. Ibrahim, and Z. Ismail, "Etched FBG coated with polyimide for simultaneous detection the salinity and temperature," *Opt. Commun.*, vol. 392, pp. 218–222, 2017.

[26] A. Iadicicco, S. Campopiano, A. Cutolo, M. Giordano, and A. Cusano, "Nonuniform thinned fiber Bragg gratings for simultaneous refractive index and temperature measurements," *IEEE Photon. Technol. Lett.*, vol. 17, no. 7, pp. 1495–1497, Jul. 2005.

[27] G. An *et al.*, "Ultra-stable D-shaped optical fiber refractive index sensor with graphene-gold deposited platform," *Plasmonics*, vol. 14, pp. 155–163, 2019.

[28] Q. Wang, X. Z. Wang, H. Song, W. M. Zhao, and J. Y. Jing, "A dual channel self-compensation optical fiber biosensor based on coupling of surface plasmon polariton," *Opt. Laser Technol.*, vol. 124, 2020, Art. no. 106002.

[29] Y. Qi, J. Zhang, Q. Feng, X. Zhang, Y. Liu, and Y. Han, "A novel high sensitivity refractive index sensor based on multi-core micro/nano fiber," *Photon. Sens.*, vol. 9, no. 3, pp. 197–204, 2019.

[30] C. Zhang, T. Ning, J. Li, L. Pei, Ch. Li, and H. Lin, "Refractive index sensor based on tapered multicore fiber," *Opt. Fiber Technol.*, vol. 33, pp. 71–76, 2017.

[31] D. A. May-Arrioja and J. R. Guzman-Sepulveda, "Highly sensitive fiber optic refractive index sensor using multicore coupled structures," *J. Lightw. Technol.*, vol. 35, no. 13, pp. 2695–2701, Jul. 2017.

[32] Z. Yang, L. Xia, S. Li, R. Qi, X. Chen, and W. Li, "Highly sensitive refractive index detection based on compact HSC-SPR structure in a microfluidic chip," *Sens. Actuators A: Phys.*, vol. 297, 2019, Art. no. 111558.

[33] N. Xie, H. Zhang, B. Liu, H. Liu, T. Liu, and C. Wang, "In-line microfiber-assisted Mach–Zehnder interferometer for microfluidic highly sensitive measurement of salinity," *IEEE Sens. J.*, vol. 18, no. 21, pp. 8767–8772, Nov. 2018.

[34] L. Zhao, B. Liu, Y. Wu, T. Sun, Y. Mao, and T. Nan, "Measurement of refractive index and temperature using balloonshaped Mach–Zehnder interferometer," *Optik*, vol. 188, pp. 115–119, 2019.

[35] Y. Zheng *et al.*, "Fiber optic Fabry–Pérot optofluidic sensor with a focused ion beam ablated microslot for fast refractive index and magnetic field measurement," *IEEE J. Sel. Top. Quantum Electron.*, vol. 23, no. 2, pp. 322–326, Mar./Apr. 2017.

[36] W. Zhang, Y. Liu, T. Zhang, D. Yang, Y. Wang, and D. Yu, "Integrated fiber-optic Fabry–Pérot interferometer sensor for simultaneous measurement of liquid refractive index and temperature," *IEEE Sens. J.*, vol. 19, no. 13, pp. 5007–5013, Jul. 2019.

[37] H. Fu *et al.*, "In-fiber quasi-Michelson interferometer based on waist-enlarged fiber taper for refractive index sensing," *IEEE Sens. J.*, vol. 15, no. 12, pp. 6869–6874, Dec. 2015.

[38] J. Wang *et al.*, "A novel fiber in-line Michelson interferometer based on end face packaging for temperature and refractive index measurement," *Optik*, vol. 194, 2019, Art. no. 163094.

[39] R. X. Tan *et al.*, "Birefringent Bragg grating in C-shaped optical fiber as a temperature-insensitive refractometer," *Sensors*, vol. 18, no 10, 2018, Art. no. 3285.

[40] Q. Zhang, L. Hu, Y. Qi, G. Liu, N. Ianno, and M. Han, "Fiber-optic refractometer based on a phase-shifted fiber Bragg grating on a side-hole fiber," *Opt. Express*, vol. 23, no. 13, pp. 16750–16759, 2015.

[41] M. del, R. Bautista-Morales, R. Martínez-Manuel, and C. A. Pineda-Arellano, "Overlapped fiber-optic Michelson interferometers for simultaneous refractive index measurement at two sensing points," *Appl. Opt.*, vol. 56, no. 34, 2017, Art. no. 9515.

[42] K. S. Park *et al.*, "Compact and multiplexible hydrogen gas sensor assisted by self-referencing technique," *Opit. Express*, vol. 19, no. 19, pp. 18190–18198, 2011.

[43] L. Liu, Y. Gong, Y. Wu, T. Zhao, H. Wu, and Y. Rao, "Spatial frequency multiplexing of fiber-optic interferometric refractive index sensors based on graded-index multimode fibers," *Sensors*, vol. 12, pp. 12377–12385, 2012.

[44] A. Van Newkirk, J. E. Antonio-Lopez, G. Salceda-Delgado, M. U. Piracha, R. Amezcua-Correa, and A. Schülzgen, “Multicore fiber sensors for simultaneous measurement of force and temperature,” *IEEE Photon. Technol. Lett.*, vol. 27, no. 14, pp. 1523–1526, Jul. 2015.
[45] G. Salceda-Delgado, A. Van Newkirk, J. E. Antonio-Lopez, A. Martinez-Rios, A. Schülzgen, and R. Amezcua Correa, “Compact fiber-optic curvature sensor based on super-mode interference in a seven-core fiber,” *Opt. Lett.* vol. 40, no. 7, pp. 1468–1471, 2015.
[46] C. Guan, X. Zhong, G. Mao, T. Yuan, J. Yang, and L. Yuan, “In-Line Mach–Zehnder interferometric sensor based on a linear five-core fiber, ” *IEEE Photon. Technol. Lett.*, vol. 27, no. 6, pp. 635–638, Mar. 2015.
[47] X. Zhan *et al.*“Few-mode multicore fiber enabled integrated Mach–Zehnder interferometers for temperature and strain discrimination,” *Opt. Express*, vol. 26, no. 12, pp. 15332–15342, 2018.
[48] J. Enrique Antonio-Lopez, Z. S. Eznaveh, P. LiKamWa, A. Schülzgen, and R. Amezcua-Correa, “Multicore fiber sensor for high-temperature applications up to 1000°C,” *Opt. Lett.* vol. 39, no. 15, pp. 4309–4312, 2014.
[49] A. W. Snyder, “Coupled-mode theory for optical fibers,” *J. Opt. Soc. Amer.*, vol. 62, no. 11, pp. 1267–1277, 1972.
[50] Y. Murakami and S. Sudo, “Coupling characteristics measurements between curved waveguides using a two-core fiber coupler,” *Appl. Opt.*, vol. 20, pp. 417–422, 1981.
[51] R. Wenhua and Z. Tan, “A study on the coupling coefficients for multi-core fibers,” *Optik*, vol. 127, no. 6, pp. 3248–3252, 2016.
[52] C. Xia *et al.*, “Supermodes in coupled multi-core waveguide structures,” *IEEE J. Sel. Top. Quantum Electron.*, vol. 22, no. 2, pp. 196–207, Mar./Apr. 2016.
[53] C. Xia, N. Bai, I. Ozdur, X. Zhou, and G. Li, “Supermodes for optical transmission,” *Opt. Express*, vol. 19, no. 17, pp. 16653–16664, 2011.
[54] A. Samir and B. Batagelj, “A seven-core-fiber spectral filter based on LP01-LP01 mode coupling,” *Optoelectron. Adv. Mater.-Rapid Commun.*, vol. 11, nos. 11/12, pp. 628–32, 2017.
[55] K. Saitoh and S. Matsuo, “Multicore fiber technology,” *J. Lightw. Technol.*, vol. 34, no. 1, pp. 55–66, 2016.
[56] J. Villatoro, A. Van Newkirk, E. Antonio-Lopez, J. Zubia, A. Schülzgen, and R. Amezcua-Correa, “Ultrasensitive vector bending sensor based on multicore optical fiber,” *Opt. Lett.*, vol. 41, no. 4, pp. 832–835, 2016.
[57] A. Perez-Leija, J. Hernandez-Herrejon, H. Moya-Cessa, A. Szameit, and D. N. Christodoulides, “Generating photon-encoded W states in multiport waveguide-array systems,” *Phys. Rev. A*, vol. 87, 2013, Art. no. 013842.
[58] R. Wenhua, T. Zhongwei, “A study on the coupling coefficients for multi-core fibers,” *Optik - Int. J. Light Electron. Opt.*, vol. 127, no. 6, pp. 3248–3252, 2016.
[59] M. D. Wales, P. Clark, K. Thompson, Z. Wilson, J. Wilson, and C. Adams, “Multicore fiber temperature sensor with fast response times,” *OSA Continuum* vol. 1, no. 2, pp. 764–771, 2018.
[60] B. E. A. Saleh and M. C. Teich, *Fundamentals of Photonics*. 2nd ed. Hoboken, NJ, USA: Wiley, 2007, p. 318.
[61] M. Born and E. Wolf, *Principles of Optics*. 7th ed. Cambridge, U.K.: Cambridge Univ. Press, 1999.
[62] O. Svelto, *Principles of Lasers*. 2th ed. Berlin, Germany: Springer, 1982.
[63] K. Y. Aldoğan and İ. D. E. Cansu, “Experimental investigation of refractive index measurement of common solvents and aqueous solutions in the infrared wavelengths,” *Balkan J. Elect. Comput. Eng.*, vol. 6, no. 3, pp. 159–164, 2018.
[64] J. E. Saunders, C. Sanders, H. Chen, and H.-P. Loock, “Refractive indices of common solvents and solutions at 1550 nm, ” *Appl. Opt.* vol. 55, no. 4, pp. 947–953, 2016.

Natanael Cuando-Espitia received the Ph.D. degree in materials science and engineering from Universidad Nacional Autonoma de Mexico, Mexico, in 2015. From 2016 to 2019, he was at the University of California Riverside, USA, as a Postdoctoral Fellow. He is currently with the Universidad de Guanajuato, Salamanca, Mexico. His current research interests include optical fiber sensors and biophotonics.

Miguel A. Fuentes-Fuentes received the B.S. degree in electronic engineering from the Instituto Tecnológico de Salina Cruz (ITSAL), Oaxaca, México, in 2009 and the M.S. and Ph.D. degrees from Instituto Nacional de Astrofísica Óptica y Electrónica (INAOE), Santa María Tonantzintla, Puebla, Mexico, in 2012 and 2017, respectively. He was a Visiting Student at the College of Optics and Photonics (CREOL), Orlando, FL, USA, in 2012 and 2013. He is currently a Postdoctoral Researcher with the Centro de Investigaciones en Óptica (CIO), Aguascalientes, México. His research interests include integrated optical devices based on long range surface plasmon polariton (LRSPP) and special optical fiber sensors.

Daniel Alberto May-Arrioja received the Ph.D. degree in optics from the College of Optics and Photonics (CREOL), University of Central Florida, Orlando, FL, USA, in 2006. He is currently a Full Time Researcher with the Fiber and Integrated Optics Laboratory, Centro de Investigaciones en Optica (CIO), Aguascalientes, Mexico. His current research interests include integrated photonics and fiber-optic devices with applications in lasers, sensors, and biosensors, and microelectromechanical systems.

Iván Hernández-Romano received the Ph.D. degree in optics from the Instituto Nacional de Astrofísica, Optica y Electronica, Puebla, Mexico, in 2011. He is currently a CONACYT Research Fellow with the Department of Electronics, DICIS, University of Guanajuato, Salamanca, Mexico. His current research interests include optical fiber sensors and their applications.

Rodolfo Martínez-Manuel received the M.Sc. and Ph.D. degrees in optics from the Ensenada Center for Scientific Research and Higher Education (CICESE), Ensenada, México, in 2004 and 2008, respectively. In 2009, he joined the Photonics Research Group, University of Johannesburg (UJ), South Africa; from 2012 to 2014, he was the Head of the Photonics Research Group, UJ. In 2015, he joined the Centro de Investigaciones en Óptica, A.C., Unidad Aguascalientes, México as a Research Scientist. His research interests are algorithm design for signal processing in sensor systems, research and development of fiber sensors, and development of fiber lasers for fiber sensors application.

Miguel Torres-Cisneros received the Ph.D. degree in physics (nonlinear optics) from the Instituto Nacional de Astrofísica, Óptica y Electrónica, Puebla, México, in 1997. He was a Visiting Researcher at Electro-optics; University of Dayton and Multiple Quantum Wells; CREOL, UCF. He is currently a member of the Applied Physics Group and a Researcher with the Electronics Department, College of Engineering, University of Guanajuato, Salamanca, Mexico. His current research interests include optical fiber sensors and their applications.